All 3-D Printed Antennas Based on Phase Velocity Control for Beam Steering and Size Reduction With Low Cost

Sheng Huang, *Graduate Student Member, IEEE*, King Yuk Chan, *Member, IEEE*, and Rodica Ramer, *Senior Member, IEEE*

***Abstract*— A concept based on engineering a dielectric filling material to adjust the phase velocity of the propagating electromagnetic wave in a horn antenna is proposed. The resulting transformation from the spherical to plane wave at the aperture is used to prove that the size reduction of the horn is achievable. The designed antenna demonstrates more than 50% size reduction with improved radiation pattern, including the sidelobe level (SLL) and satisfactory gain when compared to the commercial horn antenna. It also offers a wide bandwidth from 22 to 26.5 GHz. This design is further elaborated for a continuous, from −21° to +21°, beam steering along the electric polarization implementation by asymmetrical dielectric insertions, with a measured relative bandwidth around 27.1%. The two simple designs are liquid crystal display (LCD) 3-D printed using a commercial UV resin, with the relative permittivity $\varepsilon_r = 2.75$ and loss tangent around 0.025. The fabrication method allows easy control of the effective permittivity of dielectric–air combined units at low cost.**

***Index Terms*— Beam reconfigurable, beam steering, horn antenna, liquid crystal display (LCD) 3-D printed antennas, phase velocity.**

I. Introduction

THE demand for large transmission capacity required by modern communications and multifunctional integration attracted significant attention on the topic of reconfigurable antennas [1]–[3]. In particular, the beam-reconfigurable antennas have been developed to meet the needs of practical applications [4]–[16], representing an important continuing research direction.

The operation of the beam-steering relies on electronic or mechanical control to provide phase shift. For the electronic control, various approaches, such as the array lens and phase array excitation network, have been developed in the last few years [17]–[25]. In [19] and [20], the control of the elements of the frequency selective surfaces is applied to successfully steer the beam of a feeding horn antenna. In [21], PIN diodes between the radiating elements are utilized to achieve the beam switching and pattern reconfigurable. Another electronic solution based on a partially reflective surface excited by a phased array antenna is presented in [25]. In the case of the above, the beam-steering antennas require phase shifters to operate every single element of the antenna feeding network and the transmit array, resulting in a complex design.

The mechanical solution mainly involves the physical movement of the radiating element to provide the phase shift, for example, the rotation of the parasitic lens. Recently, a conical horn antenna with a reconfigurable beam achieved by placing an anisotropic Huygens metasurface in front of the aperture is proposed at 9 GHz in [26]. According to the measurement results, the main beam can be steered at 30° by rotating the circular metasurface with a diameter of $3.03\lambda_0$. Furthermore, the rotatable metal and dielectric lens are introduced to achieve beam steering by altering the wavefront with reduced design difficulties [27]–[30]. More recently, several beam-steering antennas have been designed in multiple technologies, including the utilization of tunable materials such as liquid crystals and the dielectric lens, aiming to reduce the design complexity. In [31], a liquid-filled lens antenna operating at V-band is proposed, with the measured steered beam from −30° to 30° along the H-field controlled by the electrode biasing network. Another beam reconfigurable Vivaldi antenna using the fluidical lens from 32 to 35 GHz is proposed in [32]. Although the beam is steered up to 25° by filling the dielectric lens with the ethyl acetate, the radiation patterns are unstable and difficult to control. New techniques, such as the mechanical control of the liquid metal parasitic to achieve the beam reconfiguration by reconstructing the radiating elements, are proposed in [33] and [34]. Nevertheless, they require high precision and fabrication cost, which may not be suitable for mass production. To realize an easy beam control, several studies on beam steering by varying the propagation constant between the radiation elements through the movable dielectric transmission line have been proposed [35]–[37]. Taken together, the major limitations of these designs are difficulties in the manufacturing process, design cost, control of the systems, and radiation performance.

In this work, we present a novel design based on engineering the phase velocity of the propagating wave in a single-horn antenna. The control of the phase velocity is realized by changing the effective permittivity of dielectric–air combined

Manuscript received April 30, 2021; revised August 24, 2021; accepted September 12, 2021. Date of publication October 14, 2021; date of current version March 3, 2022. This work was supported by the Australian Research Council under Grant DP170102939 and Grant DP200103127. *(Corresponding author: King Yuk Chan.)*

The authors are with the School of Electrical Engineering and Telecommunications, The University of New South Wales, Sydney, NSW 2052, Australia (e-mail: kyc@unsw.edu.au).

Color versions of one or more figures in this article are available at https://doi.org/10.1109/TAP.2021.3118777.

Digital Object Identifier 10.1109/TAP.2021.3118777

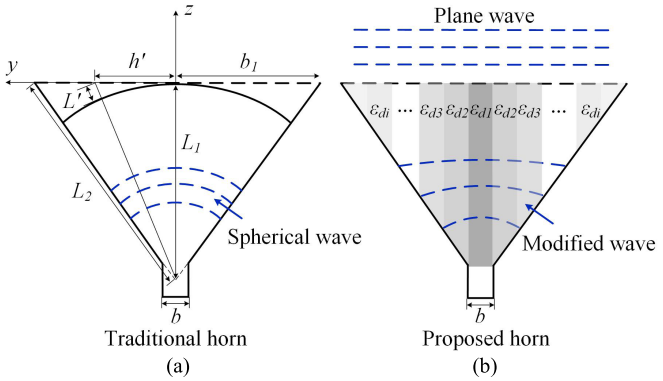

Fig. 1. Proposed concept for the plane wave at the aperture. (a) Traditional horn antenna. (b) Horn filled with progressively varied ε_d.

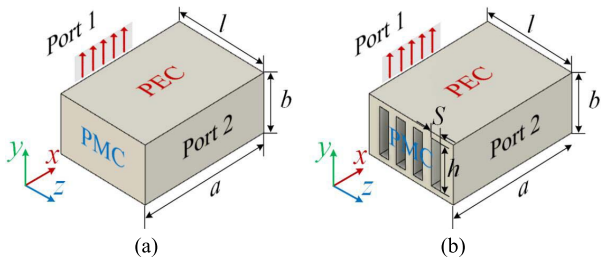

Fig. 2. Dielectric structures. (a) Dielectric-only block. (b) Dielectric–air combined unit.

TABLE I
DIMENSIONS OF THE DIELECTRIC STRUCTURES IN FIG. 2 (mm)

a	b	l	S	h
10.6	4.4	7.535	0 to 1.85	0 to 4.4

units inside the horn. Two antennas are designed and fabricated to evaluate our approach. We first present a design, which is 50% smaller in size than a commercial horn antenna and keeps a similar radiation pattern with a reduced sidelobe level (SLL). Then, a second continuous beam-steering antenna design with a simple 1-D movement of dielectric insertions is realized by modifying the field distribution in the single-horn element. The proposed approach has the advantage of reducing the manufacturing cost and design difficulty. Both proposed antenna structures are fabricated by liquid crystal display (LCD) 3-D printing using commercial light-curing resin.

This article is organized in the following way. The concept, methodology, and analysis of the proposed structure are given in Section II. In Section III, we present the design of a size-reduced antenna. The realization of the beam-steering antenna is shown in Section IV, together with the simulated results. Section V shows the details of the fabrication and the measurement of both the proposed antennas.

II. Methodology and Theoretical Analysis

A. Proposed Methodology

The geometry of a traditional horn antenna [38] and the concept of the proposed antenna utilized in this article are shown in Fig. 1(a) and (b). For the traditional horn antenna, as the spherical waves travel in the horn with the same phase velocity, the phase at the aperture varies. The geometrical path difference for any point h' over the aperture is labeled L'. Thus, the phase difference $\Delta\varphi$ over the aperture can be obtained by referring to the geometrical dimensions of the horn, as shown in (1), where k is the wavenumber and λ is the wavelength of the spherical waves in the horn. To perform the phase compensation at the aperture, the phase velocity of the waves is modified by controlling the permittivity of the dielectric material in the horn

$$\Delta\phi = kL' = \frac{\pi\left(h'\right)^2}{\lambda L_1}, \quad 0 \le h' \le b_1. \tag{1}$$

As shown in Fig. 1, to achieve the plane wave at the aperture considering the fabrication simplicity for the 3-D printing and the operating mechanism of the pattern reconfiguration, the dielectric sections with different permittivity are designed symmetrically distributed from the aperture center along the y-axis to the horn edge. If the permittivity of the dielectric sections decreases from the center to the edge of the horn, for example, $\varepsilon_{d1} > \varepsilon_{d2} > \cdots > \varepsilon_{di}$, the corresponding phase velocity in these dielectric sections increases. These will lead to the electromagnetic waves near the edge chasing the inner waves, resulting in the wave transformation from a spherical wavefront to plane wavefront in the horn aperture when proper assignments of permittivity in different dielectric sections are provided.

B. Dielectric–Air Combined Unit

For an easy understanding of the proposed antenna design, we present a comparative analysis of a "dielectric-only" block and the "dielectric–air combined" unit, as shown in Fig. 2(a) and (b), with the dimensions given in Table I, having the same overall rectangular parallelepiped size $a \times b \times l$, operating at 24 GHz. The dimensions of a and b are set the same as the WR42 waveguide, and l is about one guided wavelength when the waveguide is fully dielectric-filled. For each structure, port 1 is assigned with the plane wave excitation. The perfect electrical conductor (PEC) and perfect magnetic conductor (PMC) boundaries are assigned on the surface in xz- and yz-planes, respectively.

In terms of the phase response at port 2, for the dielectric-only block [see Fig. 2(a)], the phase delay can be controlled by the directly modified relative permittivity ε_d. For the dielectric–air combined unit [see Fig. 2(b)], the phase delay is controlled by the inserted identical air slots with $h \times S$ dimensions. The effective permittivity ε_e of such a unit can thus be decreased by increasing the proportion of the air volume in the dielectric material [39]–[41]. In our case, four uniformly distributed air slots are used for demonstration, and the effective permittivity ε_e can be calculated by using (2).

Fig. 3(a) and (b) shows the simulated phase response for the different relative permittivity ε_d of the dielectric-only block and the calculated corresponding phase velocity v_p referring to (3) and (4) [42]. The relative permittivity of the dielectric

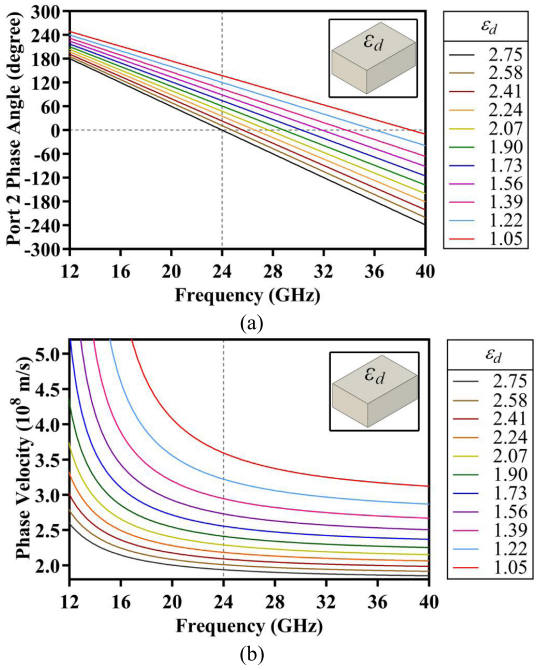

Fig. 3. Simulated phase response of dielectric-only blocks versus relative permittivity. (a) Phase angle at port 2. (b) Corresponding phase velocity.

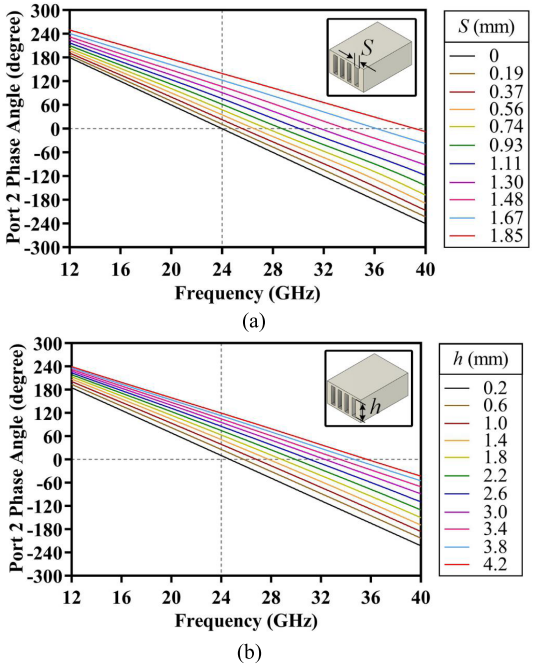

Fig. 4. Simulated phase angle response of dielectric–air combined unit (a) versus S for $h = 4.4$ mm and (b) versus h for $S = 1.88$ mm.

is varied from 2.75, the maximum value of the cured resin to a chosen 1.05 air-like value. One can see that, at the designed length l and frequency f, a maximum phase difference of about 137° can be obtained, corresponding to the maximum phase velocity difference around 1.65×10^8 m/s

$$\varepsilon_e = \frac{4hS}{bl}\varepsilon_{air} + \left(1 - \frac{4hS}{bl}\right)\varepsilon_d \tag{2}$$

$$v_p = \frac{c}{\sqrt{\varepsilon_d \mu_r}\sqrt{1 - (f_c/f)^2}} \tag{3}$$

$$f_{c10} = \frac{1}{2a\sqrt{\mu_r \varepsilon_d}}. \tag{4}$$

For the combined dielectric–air unit, the relative permittivity of the dielectric part ε_d is fixed at 2.75. Fig. 4(a) and (b) shows the phase angle for different S and h values when $h = 4.4$ mm and $S = 1.88$ mm, respectively. It can be seen that to increase the phase velocity, the proportion of the air volume should be increased by simply controlling these dimensions. At 24 GHz, a 60° phase difference with phase velocity 2.41×10^8 m/s provided by the dielectric-only block can be realized by the dielectric–air combined unit with the air slot size $S \times h = 0.93$ mm $\times$ 4.4 mm.

The initial simulation results indicate that by optimizing the proportion of the air slots in the dielectric–air combined unit, the relative permittivity of the dielectric-only block can be planned. As a result, the proposed unit is expected to vary the phase velocity of the waves in the dielectric sections, as shown in Fig. 1, compensating for the phase difference at the horn's aperture.

TABLE II
DIMENSIONS OF THE ANTENNAS IN FIG. 5 (mm)

L	W	H	L_s	W_s	H_s	S_u
18.5	14	24.4	48	29	21.6	2.5
S_1	S_2	S_3	h_1	h_2	h_3	h_u
1.45	1.85	2	3	3	3	3.5
R_1	R_2	R_3	R_4	R_5	R_6	R_7
11	11.49	11.98	12.47	12.97	13.46	13.96

III. ANTENNA DESIGN

A. Design of the Size-Reduced Antenna

1) Antenna Structure and Field Analysis: This section shows the proposed antenna design with 15 dB gain achieved by optimizing the proportion of the air slots in each dielectric section. To demonstrate the size reduction and radiation improvement, an air-filled antenna with the same dimensions as the proposed antenna and a WR-42 waveguide standard horn antenna (PE9852A-15) with nominal 15 dB gain operating from 18 to 26.5 GHz are taken as a comparison.

The geometry and the dimensions of the proposed and the standard horn antenna are shown in Fig. 5, in scale, and in Table II. The aperture dimension H is adjusted 2.8 mm larger than the standard horn H_s to achieve the similar E-plane radiation patterns and gain offered by the standard antenna. It should be noted that although $H_s < H$ by 2.8 mm, the width of the proposed antenna is $W < W_s$ by 15 mm. Considering the process of the 3-D printing fabrication technology and the physical properties of the cured resin, three dielectric sections with identical height $h_u = 3.5$ mm are designed. The lengths of all units labeled S_u are identical and set to 2.5 mm initially. For the gain enhancement fulfillment and the SLL reduction,

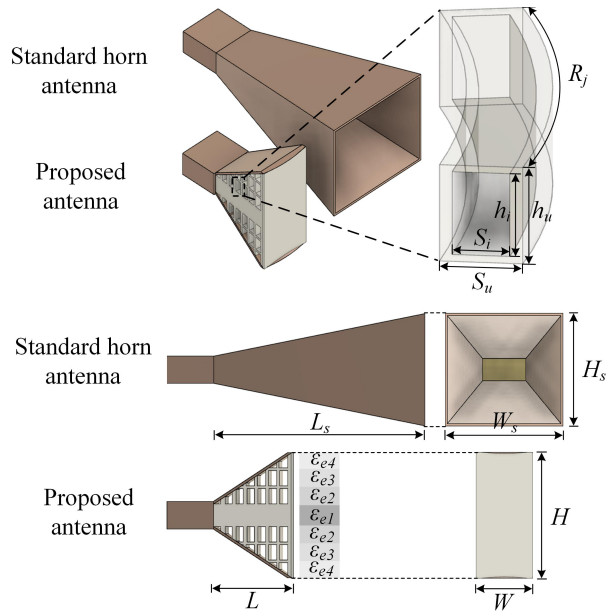

Fig. 5. Geometry of the proposed antenna and a WR-42 waveguide standard horn antenna (both achieving 15 dB gain).

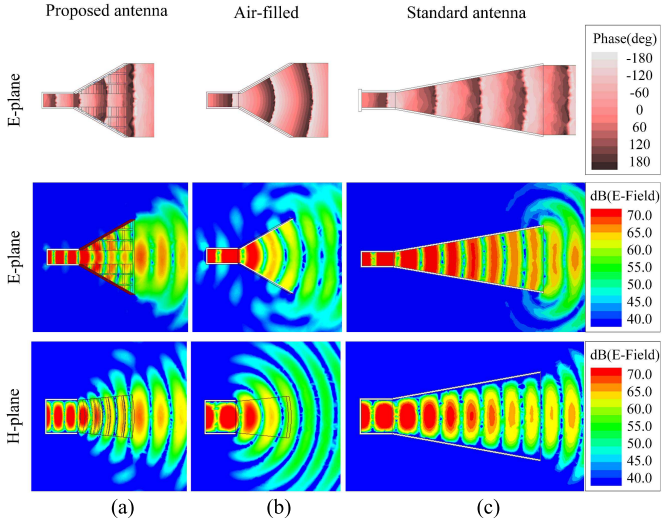

Fig. 6. Simulated phase and E-field magnitude of the three antennas. (a) Proposed antenna. (b) Air-filled antenna. (c) Standard antenna.

the optimized dimensions of the dielectric–air combined unit are given in Table II. Here, all units are designed with curved surfaces to provide the feasible geometric structure required for the beam-steering capability detailed in Section IV. The flare angle determines the length R_j of the units in the H-plane. Thus, ε_{ei} of all-dielectric sections is calculated as $\varepsilon_{e1} = \varepsilon_d = 2.75$ (the UV resin relative permittivity), $\varepsilon_{e2} = 1.83$, $\varepsilon_{e3} = 1.58$, and $\varepsilon_{e4} = 1.48$ by using (2).

The simulated phase plots in the E-plane of the proposed, air-filled, and standard antennas are shown in the first row in Fig. 6. They demonstrate the aperture phase compensation of the proposed dielectric–air combined unit obtained by the phase velocity controlled in the horn. As the permittivity

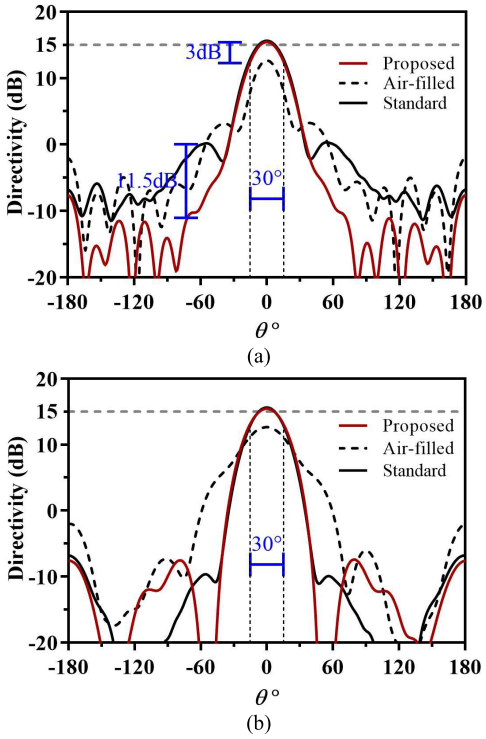

Fig. 7. Simulated radiation patterns of three antennas at 24 GHz. (a) E-plane patterns. (b) H-plane patterns.

of the dielectric sections is higher in the middle of the horn, the waves are decelerated and complete two guided wavelengths propagation, forming the plane wavefront at the aperture, as opposed to the curved wavefront of the air-filled antenna caused by the constant phase velocity of the wave.

The simulated E-field magnitude distributions of the three antennas in E- and H-planes are also given in Fig. 6. The difference in the E-field distributions in the E-plane inside the horn (second row) shows that, for the proposed antenna, the wave propagation in the first dielectric section (ε_{e1}) in the center slows due to the lowest phase velocity given by the full dielectric. As the proportion of the air volume increases gradually from the second to the fourth dielectric sections, the propagation of these waves accelerates as the effective permittivity decreases. Thus, we can see that after about one wavelength from the throat of the horn, the wave starts to transform to the plane wave. To realize the similar aperture field distribution as the proposed antenna, the standard horn antenna requires a longer horn and larger aperture to provide the uniform transition of the wave propagation.

2) Improvement of the Radiation Performance: The directivity of the three antennas operating at the same frequency are plot in Fig. 7(a) and (b). The impacts of the loss in the dielectric material and conductivity of the horn are not considered. Without any modifications to the external structure, the proposed antenna has the advantage of increasing the gain by 3 dB, compared to the air-filled antenna. When compared to the standard horn, the proposed antenna has also the advantage of reduced horn length and width, by about 61% and 46%, while maintaining the gain around 15 dB.

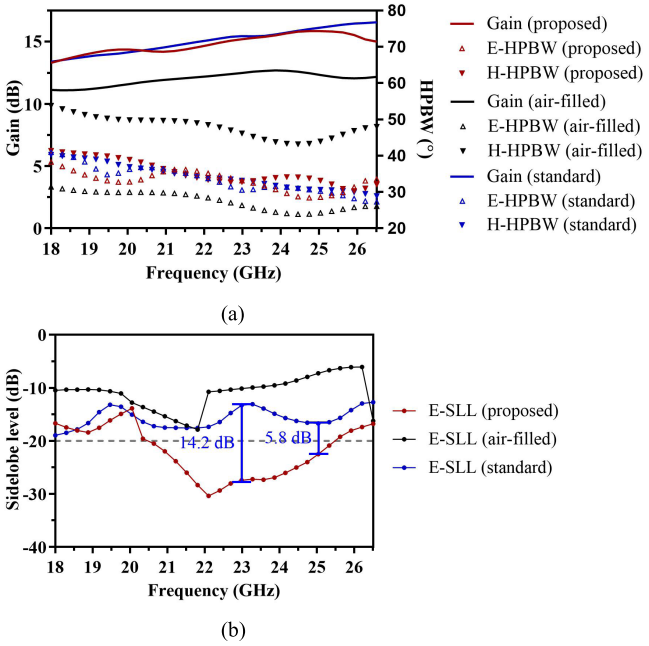

Fig. 8. Simulated radiation performance of the three antennas in K-band. (a) Gain and HPBWs. (b) SLLs in E-plane.

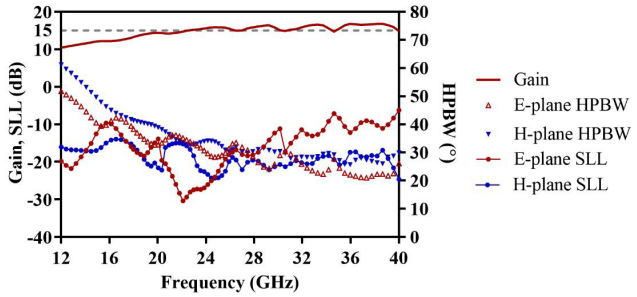

Fig. 9. Simulated radiation performance of the proposed antenna in Ku-, K-, and Ka-band.

Furthermore, the −26.9 dB SLL in E-plane is 11.5 dB lower of the standard antenna. The H-plane pattern keeps the same half-power beamwidth (HPBW) as the standard antenna. Overall, the simulated radiation results indicate that the proposed antenna can achieve gain maintenance for low SLL together with the considerable size reduction.

As shown in Fig. 8, we also compare three antennas in terms of the radiation performance at K-band. Fig. 8(a) indicates that the proposed size-reduced antenna maintained the gain as the standard antenna from 18 to 24.5 GHz. The gain decreases about 1 dB after 26 GHz as the HPBWs in both E- and H-planes increase. The comparison of the E-plane SLLs of the three antennas at the same frequency range is shown in Fig. 8(b). Much lower SLL can be achieved by the proposed antenna. Around 5–14 dB reduction of the SLL is observed between the proposed and standard antennas, from 21 to 25 GHz.

The simulated radiation performance of the proposed size-reduced antenna in Ku-, K-, and Ka-band is shown in Fig. 9, and the simulated reflection coefficient S_{11} of the three investigated antennas is shown in Fig. 10. These simulated results

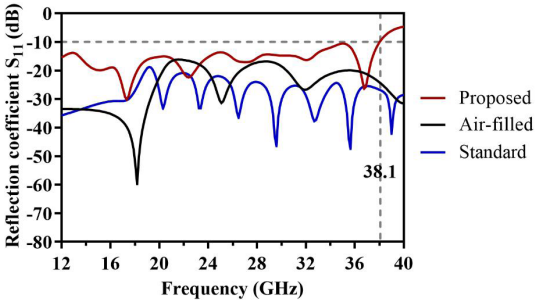

Fig. 10. Simulated reflection coefficient S_{11} of the three antennas in Ku-, K-, and Ka-band.

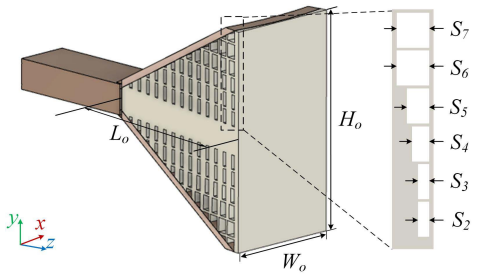

Fig. 11. Updated proposed horn with the zoomed side view of the dielectric–air sections.

TABLE III
DIMENSIONS OF THE ANTENNAS IN FIG. 11 (mm)

L_o	W_o	H_o	S_2	S_3	S_4	S_5	S_6	S_7
40	25	46	1	1	1.4	1.7	2.5	2.5

indicate that the proposed antenna can achieve a relative bandwidth of about 109% from 12 to 38.1 GHz while maintaining a good radiation pattern. From the simulated results, the proposed antenna offers a gain from 10.4 to 13 dB in Ku-band and 14.7 to 16.8 dB in Ka-band. Due to the mismatch at the frequencies beyond 38.1 GHz, the gain starts to drop to 14.8 dB at 40 GHz.

B. Design of the Beam-Steering Antenna

In our work, the direction of the beam steering is along the electric polarization. This is achieved by controlling the field distribution in the horn with asymmetrically modified effective permittivity of the dielectric–air combined unit. Thus, the beam direction can be steered along the electric field by filling the air of the horn with the dielectric material. Similar operating principles of beam steering, varying the permittivity and the propagation constant, have been reported in some recent designs [35]–[37]. It should be noted that this is the first time that such a principle is applied to steer the E-plane pattern for a single-horn element. Moreover, it is worth indicating that continuous beam steering can be realized with a simple physical operation that gradually fills the unit.

1) Antenna Structure: As shown in Fig. 11, an updated optimized proposed antenna with dimensions listed in Table III is designed at 24 GHz. The size of the horn is enlarged for a

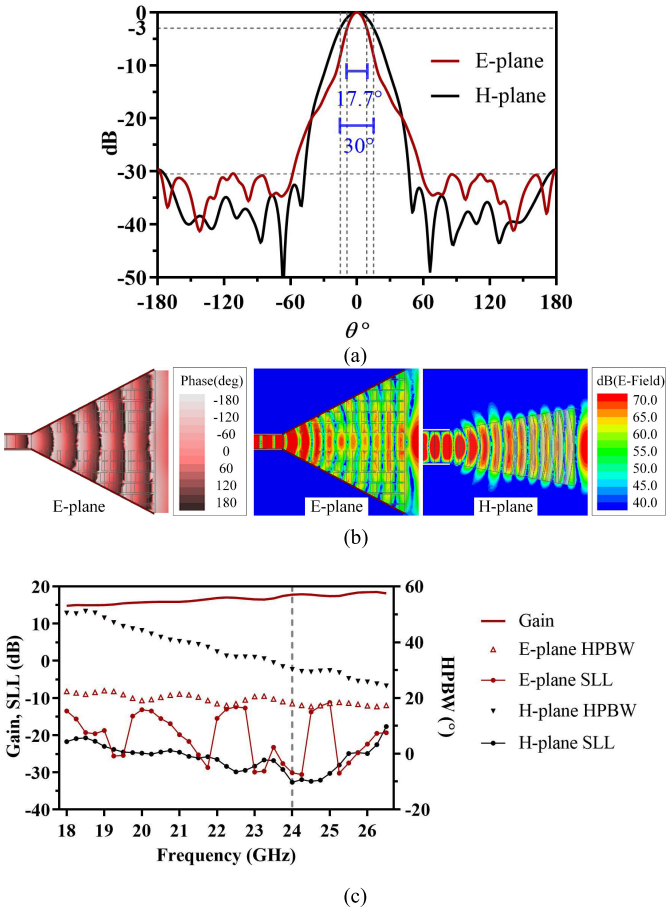

Fig. 12. Simulated radiation performance of the updated antenna. (a) Normalized radiation pattern at 24 GHz. (b) Phase and field plot at 24 GHz. (c) Radiation characteristics at K-band.

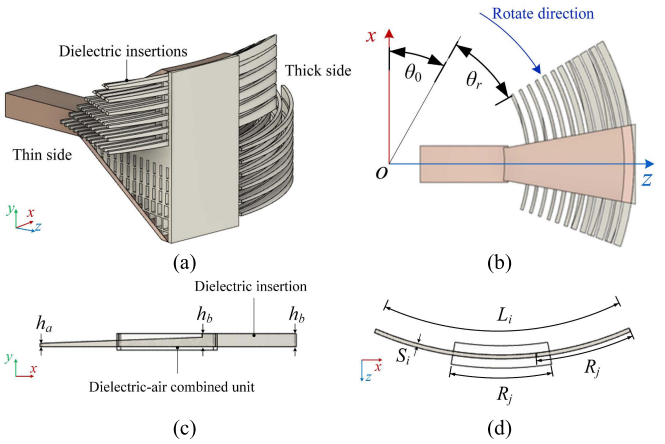

Fig. 13. Configuration of the beam steering mechanism. (a) Perspective view of the proposed antenna with the dielectric insertions. (b) Top view. (c) Front view of one unit with dielectric insertion. (d) Top view of one unit with dielectric insertion.

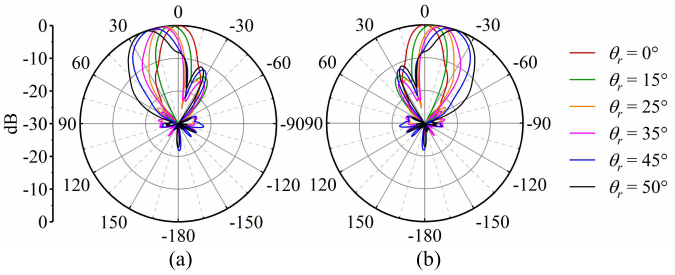

Fig. 14. Simulated normalized radiation E-plane patterns at 24 GHz for several chosen discrete rotating angles θ_r. (a) Only topside dielectric rotated insertions. (b) Only bottom side dielectric rotated insertions.

narrower E-plane beam. Six dielectric sections with modified effective permittivity are used to correct the phase at the aperture. The simulated radiation performance at the designed frequency is shown in Fig. 12(a) and the corresponding phase and magnitude field distributions are shown in Fig. 12(b). By properly controlling the phase velocity in the dielectric sections inside the horn, the E-plane HPBW at 17.7° can be obtained. Fig. 12 also indicates that at this frequency, low SLLs in E-plane at −30 dB and H-plane at −32.5 dB can be achieved, due to the enlarged aperture H_o and phase compensation. The simulated radiation performance without considering the material loss of the updated proposed antenna crossing K-band is shown in Fig. 12(c). The HPBWs in two planes reduce as the frequency increases, leading to an increasing gain from 14.8 to 18.2 dB.

To realize the modification of the effective permittivity in the dielectric–air combined unit, dielectric insertions are designed, as shown in Fig. 13(a) and (b). These insertions follow the same shape of the air part of the unit, including the angle and the length S_i of the corresponding air gap [see Fig. 13(c)]. As shown in Fig. 13(d), the thickness of the insertion increases from one side to another side. As the dielectric insertion advances through the air slot, the effective permittivity of the dielectric–air combined unit is modified. In this way, continuous beam steering can be achieved as the proportion of the air decreases when the thickness of the dielectric insertions in the unit increases gradually. Considering the physical properties including the hardness and flexural strength, all dielectric insertions are designed with the thin thickness $h_a = 0.76$ mm and the thick thickness h_b which equals the corresponding height of the slot. Furthermore, the curve lengths L_i of all insertions are 0.87π to the corresponding radii.

2) Simulated Steering Performance: For a clear demonstration of the beam-steering design, we define two angles, the initial angle θ_0, and rotation angle θ_r, in cylindrical coordinate, as shown in Fig. 13(b). The origin is set to the center of the circles formed by the unit (or dielectric insertions). The initial angle is defined as the maximum angle from the positive x-axis to the z-axis when the units are not filled. In this case, the maximum initial angle is $\theta_0 = 30°$. Then, the rotation angle θ_r can be used for rotating the dielectric insertions and calculating the effective permittivity inside the horn by the proportion of the dielectric in the unit.

The steered E-plane patterns at 24 GHz are emphasized in Fig. 14, where (a) and (b) show discrete states of θ_r when only top and only bottom side dielectric insertions are rotated, respectively. It can be seen that by asymmetrically controlling the effective permittivity of the dielectric–air combined units

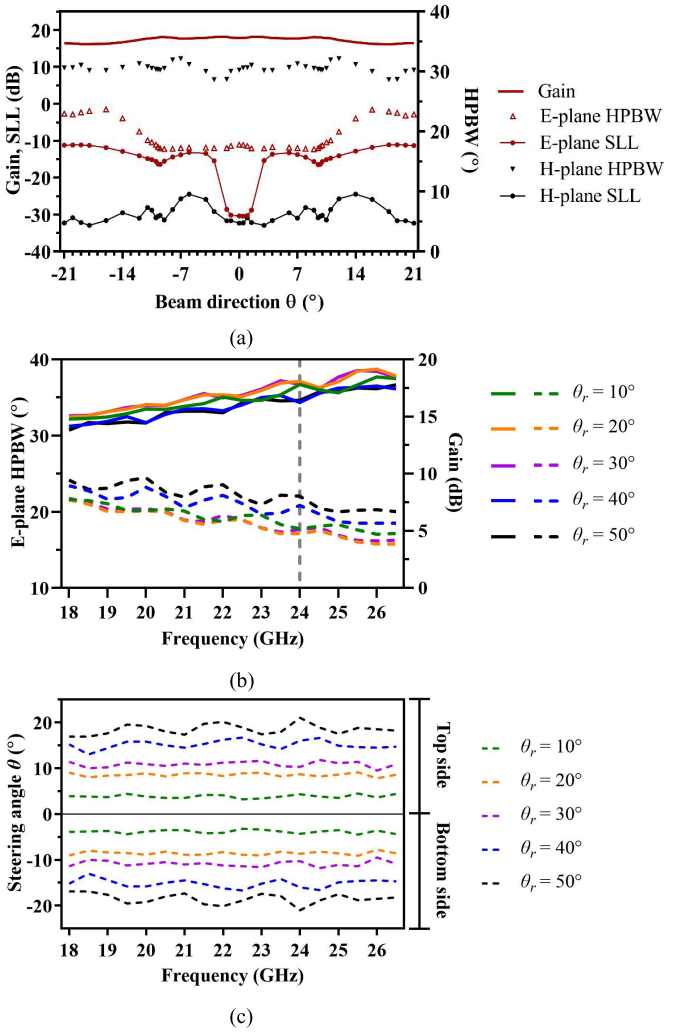

Fig. 15. Simulated radiation characteristics of the proposed beam-steering antenna. (a) Radiation characteristics versus the beam direction from −21° to 21° at 24 GHz. (b) Gain and E-plane HPBW versus the rotation angle θ_r in K-band. (c) Steering angle versus the rotation angle θ_r in K-band.

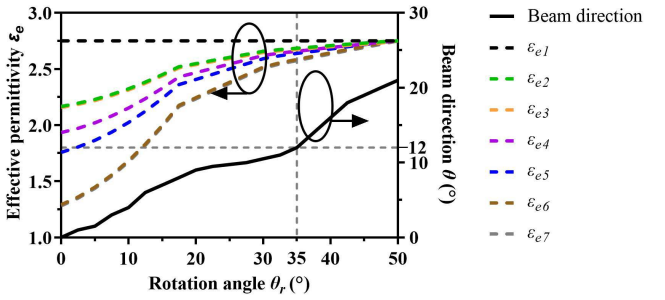

Fig. 16. Relation between the modified effective permittivity and the beam-steering angle by rotating the dielectric insertions on one side.

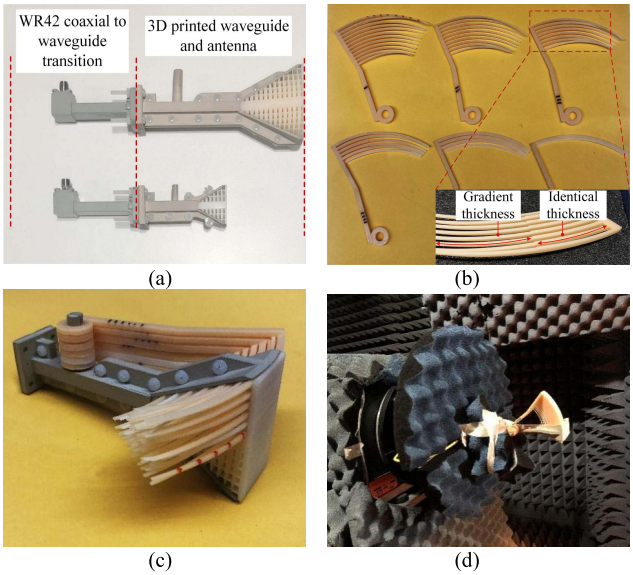

Fig. 17. Antenna fabrication and measurement. (a) 3-D printed antenna prototypes. (b) 3-D printed dielectric insertions. (c) Assembled beam-steering antenna prototype. (d) Antenna measurement set up.

on both sides, the steered beam along the electric polarization can be achieved. The maximum steering angle at ±21° is observed for $\theta_r = 50°$ when the units on either side are fully infilled.

The simulated radiation characteristics versus different beam directions from −21° to 21° with the flat gain in all directions at 24 GHz are shown in Fig. 15(a). Around a 1.3 dB drop occurs around 16° due to the broader HPBW in E-plane. Fig. 15 also shows that the H-plane pattern stays the same when the E-plane beam steers. A slight difference in SLL in the H-plane occurs because of the asymmetrical distributions of dielectric insertions. This can be further improved by increasing the curvature length of the insertions to reduce the thickness difference of the dielectric part in the air slot.

Fig. 16 shows the relation between the modified effective permittivity in each dielectric section and the beam-steering angle by rotating the dielectric insertions. When the insertions are gradually rotated, the steering angle can be increased almost linearly. For a certain beam-steering angle, the distribution of the modified effective permittivity can be calculated based on a certain rotation angle. For example, a steering angle at 12° can be offered by the modified effective permittivity with $\varepsilon_{e2} = 2.67$, $\varepsilon_{e3} = 2.67$, and $\varepsilon_{e4} = 2.66$, $\varepsilon_{e5} = 2.64$, $\varepsilon_{e6} = 2.58$, and $\varepsilon_{e7} = 2.58$ corresponding to a 35° rotation angle. It is worth noting that in this work, the transition from low to high permittivity is only provided by the insertion's thickness. A smoother transition is expected to be obtained by increasing the number of the dielectric sections or a 2-D transformation of the insertion structure with a higher resolution printing fabrication.

IV. Antenna Fabrication and Measurement

A. Fabrication

The Phrozen Sonic XL 4K LCD 3-D printer is used to fabricate the proposed size reduced and beam-steering antennas. Fig. 17(a) shows the fabricated antenna prototypes where the horns are fabricated by the same printing process synchronously. Liquid, photopolymer resin, is used to print all structures. The surface of the horn and the waveguide are metalized by a conductive spray MG Chemicals 843AR

TABLE IV
FABRICATION DETAILS OF THE PROPOSED ANTENNAS

Antenna part	Horn & waveguide		Dielectric section		
	Size-reduced antenna	Beam-steering antenna	Size-reduced antenna	Beam-steering antenna	Insertion
Building layers	720	2120	530	1067	60
Cure time per layer (ms)	3500	3500	3000	3000	3000
Thickness per layer (μm)	50	50	50	50	50
Total building time (hrs)	3.2	9.1	2.4	4.6	0.3
Consumption of resin (gram)	2.58	11.6	2.7	15.9	10.2
Total cost (USD)	0.1	0.5	0.1	0.7	0.6

Super Shield Silver Coated Copper Conductive Coating with a resistivity of 1.0×10^{-4} $\Omega \cdot$ cm. For a more accurate measurement of the proposed antennas, we measured the dielectric properties of the cured resin, including the relative permittivity by comparing the phase response between an air-filled and a dielectric-filled waveguide of the same size, and the loss tangent. A PNA network analyzer E8364C (10 MHz–50 GHz) was used. The measured relative permittivity is around 2.75 and the loss tangent is around 0.025 at 24 GHz.

The summary of the fabrication details and material cost of both antennas using the LCD printing process is given in Table IV. The total fabrication cost of a single antenna element using commercial resin is around 1 USD. All antenna parts can be simultaneously 3-D printed with the maximum building time of fewer than 10 h using the highest precision. For the beam-steering antenna, the total fabrication time of the horn and waveguide can be further shortened by reducing the building layers in a horizontally chosen printing direction.

B. Measurement Results

In the measurement, both antennas are fed with coaxial cables, and the WR42 coaxial to waveguide transition is used for the connection, as shown in Fig. 17. The measured radiation characteristics and reflection coefficient S_{11} of the proposed size-reduced antenna from 22 to 26.5 GHz are shown in Fig. 18. The maximum measured gain is 10.9 dB at 23.9 GHz. The decrease of the measured gain is due to the loss tangent of the photopolymer resin. In this frequency range, the measured gain is around 4–7 dB lower than the simulated results without considering the dielectric loss.

The measured and simulated normalized radiation patterns at 22, 24, and 26.5 GHz shown in Fig. 19 are in agreement. The difference between the simulated and measured patterns appearing in the side lobes is mainly due to the printing accuracy and cleaning process. First, as the structures are printed layer by layer, the exposure time and the speed of the movement of the base plate will cause inaccuracy of the final dimensions. Moreover, the uncured resin could remain inside the dielectric–air combined unit when the isopropyl alcohol is

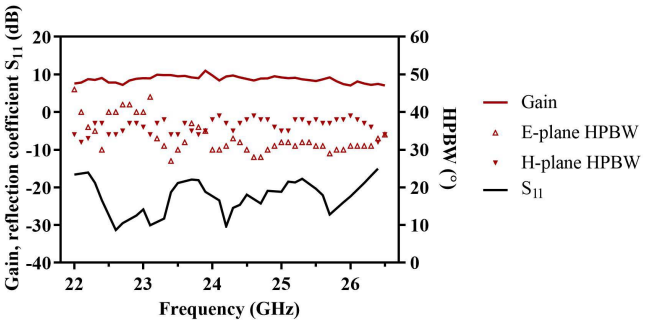

Fig. 18. Measured radiation performance and reflection coefficient S_{11} of the size-reduced antenna from 22 to 26.5 GHz.

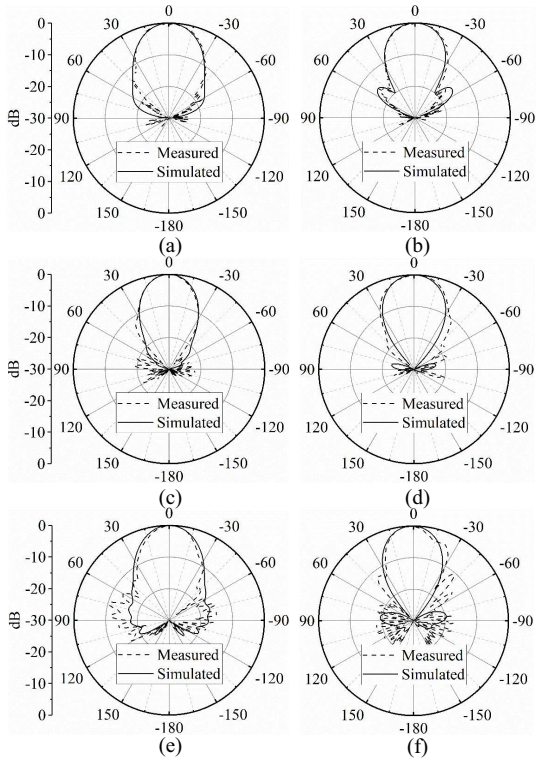

Fig. 19. Measured and simulated normalized radiation patterns of the proposed size-reduced antenna. (a) E-plane at 22 GHz. (b) H-plane at 22 GHz. (c) E-plane at 24 GHz. (d) H-plane at 24 GHz. (e) E-plane at 26.5 GHz. (f) H-plane at 26.5 GHz.

used to wash the printed structures. This also may lead to the change of the dimensions after the final curing process.

As the E-plane beam is steered symmetrically, we show one side of the measured results at six states at 24 GHz of the rotation angle θ_r in Fig. 20. The corresponding E-field distributions are also presented. The summary of the measured and simulated radiation characteristics of these states at design frequency is listed in Table V. The loss tangent of the dielectric material is considered in the simulation. The maximum measured steering angle at 20° is obtained for $\theta_r = 50°$. Due to the more dielectric material used in the beam-steering antenna design, the measured gain is lower than the simulations. As we slightly reduce the dimension S_i of the

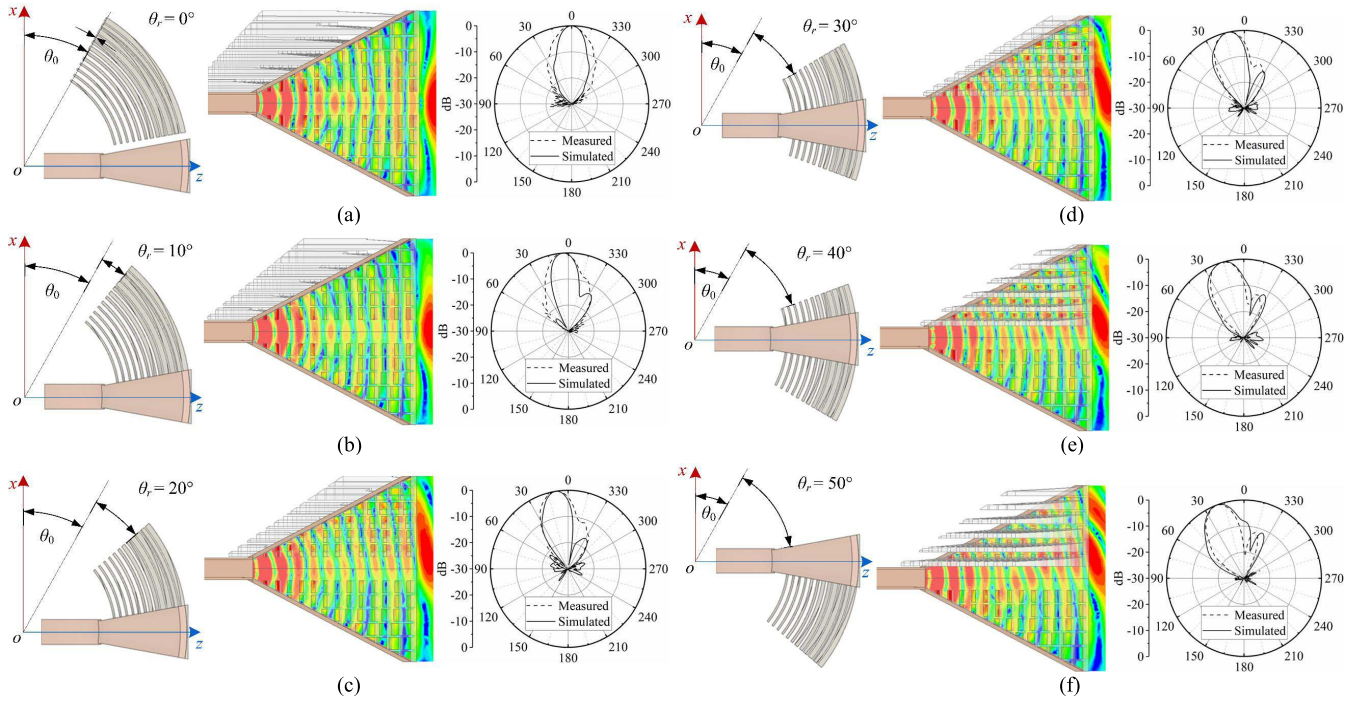

Fig. 20. Measured and simulated normalized radiation patterns with the corresponding simulated E-plane field distribution for six states at 24 GHz. (a) $\theta_r = 0°$. (b) $\theta_r = 10°$. (c) $\theta_r = 20°$. (d) $\theta_r = 30°$. (e) $\theta_r = 40°$. (f) $\theta_r = 50°$.

TABLE V
MEASUREMENT RESULTS OF THE BEAM-STEERING ANTENNA AT 24 GHz

θ_r (°)	Beam direction θ (°)		HPBW (°)		Gain (dB)		SLL (dB)	
	Sim	Mea	Sim	Mea	Sim	Mea	Sim	Mea
0	0	0	17.7	18	10.4	9.9	-30.4	-23.4
10	4	4	17.3	17.5	10.2	9.8	-13.5	-8.7
20	8	7	17.1	17.3	10.6	9.3	-15.3	-11
30	10	9	18.2	20	10.4	9.6	-15.1	-12.1
40	16	15	23.7	23	9.2	9.3	-11.8	-12.6
50	21	20	22.9	22	9.0	8.9	-11.2	-11.8

dielectric insertions to allow the movement in the slots, leading to a lower effective permittivity than the ideal case. Thus, the measured beam directions at different states have a slight shift around 1°.

The measured reflection coefficient S_{11} and the steering angle in six states at different frequencies from 20 to 26.5 GHz are shown in Fig. 21(a) and (b). For the relative bandwidth, S_{11} is below -10 dB of all states, covering the entire frequency range. The measured gain at different states shows that the drop of the gain is little because the beamwidths are kept stable. The maximum gain drop around 2 dB is measured at 22.6 GHz between $\theta_r = 0°$ and 10°.

The measured beam directions at different frequencies reveal that the proposed beam-steering antenna can successfully work at multiple frequencies. The average maximum steered angle at 20° can be achieved with the peak 23° steered angle at 23.6 GHz and the smallest 18° steered angle at 26.2 GHz. As mentioned before, the main factor contributing the gain drop in our design is the dielectric loss of the cured resin. This loss could be minimized by the developed polyimides reported in [43] and [44], where the dissipation factor is expected to reduce close to 0.002, thereby further improving the gain.

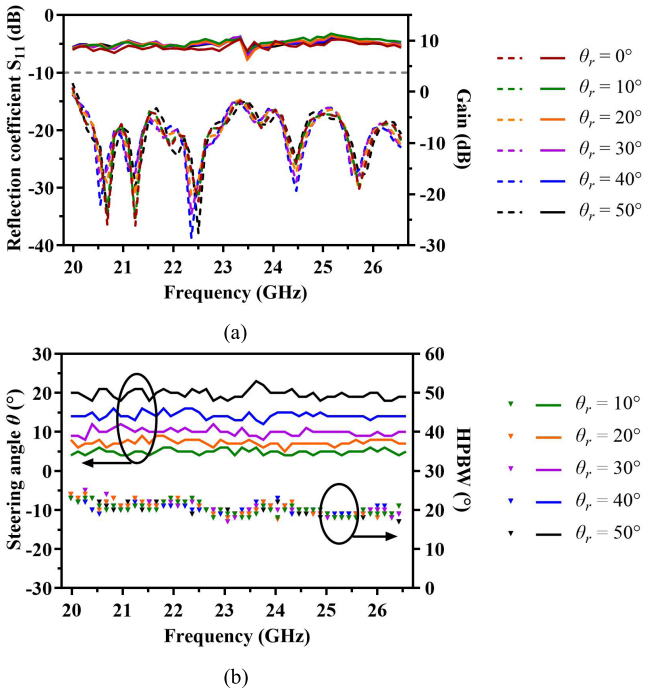

Fig. 21. Measured results of the beam-steering antenna at multiple frequencies. (a) Reflection coefficient S_{11} from 20 to 26.5 GHz. (b) Steering performance from 20 to 26.5 GHz of the proposed beam-steering antenna for different θ_r from 0° to 50°.

V. Conclusion

In this article, we present two entirely 3-D printed antennas that achieve both size reduction and continuous beam steering by the modification of the phase velocity of the propagation wave in a single-horn element. The new design concept and the operating principle are provided with the following advantages. The antenna size can be over 50% reduced in size compared to the standard horn antenna. A continuous beam steering along the E-plane is achieved in a single structure through a simple operating principle where the beam-steering antenna is realized by a rotation of dielectric insertions in one plane without the complex design of any array feeding or array lens network. The proposed design concept offers a feasible solution for engineering the elements inside the antenna. Low fabrication cost and design simplicity are achieved as the LCD 3-D printing technique is utilized. The future work may involve new composition of the dielectric material to further reduce the loss tangent and increase the permittivity that contributes to the gain improvement and narrower radiation pattern.

References

[1] S. V. Hum and J. Perruisseau-Carrier, "Reconfigurable reflectarrays and array lenses for dynamic antenna beam control: A review," *IEEE Trans. Antennas Propag.*, vol. 62, no. 1, pp. 183–198, Jan. 2014.

[2] R. L. Haupt and M. Lanagan, "Reconfigurable antennas," *IEEE Antennas Propag. Mag.*, vol. 55, no. 1, pp. 49–61, Feb. 2013.

[3] G. Oliveri, D. H. Werner, and A. Massa, "Reconfigurable electromagnetics through metamaterials—A review," *Proc. IEEE*, vol. 103, no. 7, pp. 1034–1056, Jul. 2015.

[4] H. A. Majid, M. K. A. Rahim, M. R. Hamid, and M. F. Ismail, "Frequency and pattern reconfigurable slot antenna," *IEEE Trans. Antennas Propag.*, vol. 62, no. 10, pp. 5339–5343, Oct. 2014.

[5] J.-S. Row and C.-W. Tsai, "Pattern reconfigurable antenna array with circular polarization," *IEEE Trans. Antennas Propag.*, vol. 64, no. 4, pp. 1525–1530, Apr. 2016.

[6] X. Yi, L. Huitema, and H. Wong, "Polarization and pattern reconfigurable cuboid quadrifilar helical antenna," *IEEE Trans. Antennas Propag.*, vol. 66, no. 6, pp. 2707–2715, Jun. 2018.

[7] S. A. Rezaeieh, A. Zamani, and A. M. Abbosh, "Pattern reconfigurable wideband loop antenna for thorax imaging," *IEEE Trans. Antennas Propag.*, vol. 67, no. 8, pp. 5104–5114, Aug. 2019.

[8] Y.-Y. Bai, S. Xiao, M.-C. Tang, Z.-F. Ding, and B.-Z. Wang, "Wide-angle scanning phased array with pattern reconfigurable elements," *IEEE Trans. Antennas Propag.*, vol. 59, no. 11, pp. 4071–4076, Nov. 2011.

[9] D. Rodrigo, B. A. Cetiner, and L. Jofre, "Frequency, radiation pattern and polarization reconfigurable antenna using a parasitic pixel layer," *IEEE Trans. Antennas Propag.*, vol. 62, no. 6, pp. 3422–3427, Jun. 2014.

[10] L. D. Palma, A. Clemente, L. Dussopt, R. Sauleau, P. Potier, and P. Pouliguen, "Circularly-polarized reconfigurable transmitarray in Ka-band with beam scanning and polarization switching capabilities," *IEEE Trans. Antennas Propag.*, vol. 65, no. 2, pp. 529–540, Feb. 2017.

[11] Z. Chen and H. Wong, "Wideband glass and liquid cylindrical dielectric resonator antenna for pattern reconfigurable design," *IEEE Trans. Antennas Propag.*, vol. 65, no. 5, pp. 2157–2164, May 2017.

[12] Z. Li, D. Rodrigo, L. Jofre, and B. A. Cetiner, "A new class of antenna array with a reconfigurable element factor," *IEEE Trans. Antennas Propag.*, vol. 61, no. 4, pp. 1947–1955, Apr. 2013.

[13] F. Diaby, A. Clemente, R. Sauleau, K. T. Pham, and L. Dussopt, "2 bit reconfigurable unit-cell and electronically steerable transmitarray at Ka band," *IEEE Trans. Antennas Propag.*, vol. 68, no. 6, pp. 5003–5008, Jun. 2020.

[14] C. Fan, B. Wu, Y. Hu, Y. Zhao, and T. Su, "Millimeter-wave pattern reconfigurable Vivaldi antenna using tunable resistor based on graphene," *IEEE Trans. Antennas Propag.*, vol. 68, no. 6, pp. 4939–4943, Jun. 2020.

[15] Y. Ji, L. Ge, J. Wang, Q. Chen, W. Wu, and Y. Li, "Reconfigurable phased-array antenna using continuously tunable substrate integrated waveguide phase shifter," *IEEE Trans. Antennas Propag.*, vol. 67, no. 11, pp. 6894–6908, Nov. 2019.

[16] C. Gu *et al.*, "Compact smart antenna with electronic beam-switching and reconfigurable polarizations," *IEEE Trans. Antennas Propag.*, vol. 63, no. 12, pp. 5325–5333, Dec. 2015.

[17] L. Zhang, Q. Wu, and T. A. Denidni, "Electronically radiation pattern steerable antennas using active frequency selective surfaces," *IEEE Trans. Antennas Propag.*, vol. 61, no. 12, pp. 6000–6007, Dec. 2013.

[18] C. Gu *et al.*, "3-D coverage beam-scanning antenna using feed array and active frequency-selective surface," *IEEE Trans. Antennas Propag.*, vol. 65, no. 11, pp. 5862–5870, Nov. 2017.

[19] W. Pan, C. Huang, P. Chen, M. Pu, X. Ma, and X. Luo, "A beam steering horn antenna using active frequency selective surface," *IEEE Trans. Antennas Propag.*, vol. 61, no. 12, pp. 6218–6223 Dec. 2013.

[20] J. R. Reis *et al.*, "FSS-inspired transmitarray for two-dimensional antenna beamsteering," *IEEE Trans. Antennas Propag.*, vol. 64, no. 6, pp. 2197–2206, Jun. 2016.

[21] P.-Y. Qin, Y. J. Guo, and C. Ding, "A beam switching quasi-Yagi dipole antenna," *IEEE Trans. Antennas Propag.*, vol. 61, no. 10, pp. 4891–4899, Oct. 2013.

[22] X. Ding, Y.-F. Cheng, X.-S. Yang, B.-Z. Wang, and D. E. Anagnostou, "A flush-mounted quasi-full-space beam-scanning cylindrical phased array," *IEEE Trans. Antennas Propag.*, vol. 67, no. 7, pp. 4883–4888, Jul. 2019.

[23] X. G. Zhang, W. X. Jiang, H. W. Tian, Z. X. Wang, Q. Wang, and T. J. Cui, "Pattern-reconfigurable planar array antenna characterized by digital coding method," *IEEE Trans. Antennas Propag.*, vol. 68, no. 2, pp. 1170–1175, Feb. 2020.

[24] R. Rodriguez-Cano, S. Zhang, K. Zhao, and G. F. Pedersen, "mm-wave beam-steerable endfire array embedded in a slotted metal-frame LTE antenna," *IEEE Trans. Antennas Propag.*, vol. 68, no. 5, pp. 3685–3694, May 2020.

[25] L.-Y. Ji, Y. J. Guo, P.-Y. Qin, S.-X. Gong, and R. Mittra, "A reconfigurable partially reflective surface (PRS) antenna for beam steering," *IEEE Trans. Antennas Propag.*, vol. 63, no. 6, pp. 2387–2395, Jun. 2015.

[26] X. Wan, L. Zhang, S. L. Jia, J. Y. Yin, and T. J. Cui, "Horn antenna with reconfigurable beam-refraction and polarization based on anisotropic Huygens metasurface," *IEEE Trans. Antennas Propag.*, vol. 65, no. 9, pp. 4427–4434, Sep. 2017.

[27] G.-B. Wu, K. F. Chan, S.-W. Qu, and C. H. Chan, "A 2-D beam-scanning Bessel launcher for terahertz applications," *IEEE Trans. Antennas Propag.*, vol. 68, no. 8, pp. 5893–5903, Aug. 2020.

[28] A. A. Baba, R. M. Hashmi, K. P. Esselle, M. Attygalle, and D. Borg, "A millimeter-wave antenna system for wideband two-dimensional beam steering," *IEEE Trans. Antennas Propag.*, vol. 68, no. 5, pp. 3453–3464, May 2020.

[29] I. Aghanejad, H. Abiri, and A. Yahaghi, "Design of high-gain lens antenna by gradient-index metamaterials using transformation optics," *IEEE Trans. Antennas Propag.*, vol. 60, no. 9, pp. 4074–4081, Sep. 2012.

[30] N. Gagnon and A. Petosa, "Using rotatable planar phase shifting surfaces to steer a high-gain beam," *IEEE Trans. Antennas Propag.*, vol. 61, no. 6, pp. 3086–3092, Jun. 2013.

[31] R. Reese *et al.*, "A millimeter-wave beam-steering lens antenna with reconfigurable aperture using liquid crystal," *IEEE Trans. Antennas Propag.*, vol. 67, no. 8, pp. 5313–5324, Aug. 2019.

[32] I. Goode and C. E. Saavedra, "Millimeter-wave beam-steering antenna using a fluidically reconfigurable lens," *IEEE Trans. Antennas Propag.*, vol. 69, no. 2, pp. 683–688, Feb. 2021.

[33] V. T. Bharambe and J. J. Adams, "Planar 2-D beam steering antenna using liquid metal parasitics," *IEEE Trans. Antennas Propag.*, vol. 68, no. 11, pp. 7320–7327, Nov. 2020.

[34] V. T. Bharambe, J. Ma, M. D. Dickey, and J. J. Adams, "RESHAPE: A liquid metal-based reshapable aperture for compound frequency, pattern, and polarization reconfiguration," *IEEE Trans. Antennas Propag.*, vol. 69, no. 5, pp. 2581–2594, May 2021.

[35] N. K. Host, C.-C. Chen, J. L. Volakis, and F. A. Miranda, "Ku-band traveling wave slot array scanned via positioning a dielectric plunger," *IEEE Trans. Antennas Propag.*, vol. 63, no. 12, pp. 5475–5483, Dec. 2015.

[36] A. Ghasemi and J.-J. Laurin, "A continuous beam steering slotted waveguide antenna using rotating dielectric slabs," *IEEE Trans. Antennas Propag.*, vol. 67, no. 10, pp. 6362–6370, Oct. 2019.

[37] A. H. Naqvi and S. Lim, "A beam-steering antenna with a fluidically programmable metasurface," *IEEE Trans. Antennas Propag.*, vol. 67, no. 6, pp. 3704–3711, Jun. 2019, doi: 10.1109/TAP.2019.2905690.
[38] C. A. Balanis, *Antenna Theory: Analysis and Design*, 3rd ed. New York, NY, USA: Wiley, 2005.
[39] M. Li and N. Behdad, "Wideband true-time-delay microwave lenses based on metallo-dielectric and all-dielectric lowpass frequency selective surfaces," *IEEE Trans. Antennas Propag.*, vol. 61, no. 8, pp. 4109–4119, Aug. 2013.
[40] Y.-X. Zhang, Y.-C. Jiao, and S.-B. Liu, "3-D-printed comb mushroom-like dielectric lens for stable gain enhancement of printed log-periodic dipole array," *IEEE Trans. Antennas Propag.*, vol. 17, no. 11, pp. 2099–2103, Nov. 2018.
[41] Z. Tao, W. X. Jiang, H. F. Ma, and T. J. Cui, "High-gain and high-efficiency GRIN metamaterial lens antenna with uniform amplitude and phase distributions on aperture," *IEEE Trans. Antennas Propag.*, vol. 66, no. 1, pp. 16–22, Jan. 2018.
[42] D. M. Pozar, *Microwave Engineering*, 3rd ed. Hoboken, NJ, USA: Wiley, 2005.
[43] H. Araki, Y. Kiuchi, A. Shimada, H. Ogasawara, M. Jukei, and M. Tomikawa, "Low permittivity and dielectric loss polyimide with patternability for high frequency applications," in *Proc. IEEE 70th Electron. Compon. Technol. Conf. (ECTC)*, Jun. 2020, pp. 635–640.
[44] G. E. Ponchak and A. N. Downey, "Characterization of thin film microstrip lines on polyimide," *IEEE Trans. Compon., Packag., Manuf. Technol. B, Adv. Packag.*, vol. 21, no. 2, pp. 171–176, May 1998.

Sheng Huang (Graduate Student Member, IEEE) was born in Chongqing, China. He received the B.S. degree from the Chongqing University of Posts and Telecommunications, Chongqing, in 2013, and the M.S. degree from The University of New South Wales, Sydney, NSW, Australia, in 2017, where he is currently pursuing the Ph.D. degree in electrical engineering.

His current research interests include millimeter wave antennas, substrate-integrated waveguide antennas, 3-D printed antennas, and reconfigurable antennas.

King Yuk (Eric) Chan (Member, IEEE) received the B.E., M.E., and Ph.D. degrees from the School of Electrical Engineering and Telecommunications, The University of New South Wales (UNSW), Sydney, NSW, Australia, in 2005, 2007, and 2011, respectively.

From 2008 to 2009, he was a Research Assistant with the Centre for Integrated RF Engineering (CIRFE), University of Waterloo (UW), Waterloo, ON, Canada. From 2011 to 2013, he was a Post-Doctoral Fellow with the Information and Communications Technology (ICT) Centre, CSIRO, Marsfield, NSW, Australia, where he was involved in industrial research projects. Since 2014, he has been working with the School of Electrical Engineering and Telecommunications, UNSW, where he is currently a Lecturer. His research focuses on the design, characterization, and fabrication of front-end devices with operating frequencies ranging from RF to terahertz.

Rodica Ramer (Senior Member, IEEE) received the B.E., M.E., and Ph.D. degrees in solid-state physics from the University of Bucharest, Bucharest, Romania, in 1988, 1988, and 1992, respectively.

She has been the Senior Research Scientist of the Microwave Laboratory, National Centre for Nuclear Energy of Romania. She has been a Visiting Professor and a Research Associate with the Superconductivity Laboratory, University of Alabama, Huntsville, AL, USA; the Microwave and Magnetics Laboratory, Colorado State University, Fort Collins, CO, USA; and the University of Oklahoma, Norman, OK, USA. Since 1993, she has been with the School of Electrical Engineering and Telecommunications, The University of New South Wales, Sydney, NSW, Australia, where she is currently a Full Professor and the Head of the Microelectronics and Micro/Nano-Systems Research Discipline. During that time, she spent sabbatical periods as a Visiting Professor at the Microwave Laboratory, Chiba University, Chiba, Japan, and the Antenna Electromagnetics Laboratory, National Taiwan University, Taipei, Taiwan. She has authored or coauthored more than 200 publications in the areas of the microwave, millimeter-wave circuits and materials, and EM techniques. She holds patents related to microwave waveguide devices and antennas. Her current research interests include RF MEMS, tunable millimeter-wave structures, and radio-wave propagation for wireless devices and biomedical applications.